

ARTICLE

Open Access

Aluminum scandium nitride thin-film bulk acoustic resonators for 5G wideband applications

Yang Zou¹, Chao Gao¹, Jie Zhou¹, Yan Liu¹, Qinwen Xu¹, Yuanhang Qu¹, WenJuan Liu^{1,2}, Jeffrey Bo Woon Soon^{2,3}, Yao Cai^{1,2}✉ and Chengliang Sun^{1,2}✉

Abstract

Bulk acoustic wave (BAW) filters have been extensively used in consumer products for mobile communication systems due to their high performance and standard complementary metal-oxide-semiconductor (CMOS) compatible integration process. However, it is challenging for a traditional aluminum nitride (AlN)-based BAW filter to meet several allocated 5G bands with more than a 5% fractional bandwidth via an acoustic-only approach. In this work, we propose an $\text{Al}_{0.8}\text{Sc}_{0.2}\text{N}$ -based film bulk acoustic wave resonator (FBAR) for the design of radio frequency (RF) filters. By taking advantage of a high-quality $\text{Al}_{0.8}\text{Sc}_{0.2}\text{N}$ thin film, the fabricated resonators demonstrate a large K_{eff}^2 of 14.5% and an excellent figure of merit (FOM) up to 62. The temperature coefficient of frequency (TCF) of the proposed resonator is measured to be -19.2 ppm/°C, indicating excellent temperature stability. The fabricated filter has a center frequency of 4.24 GHz, a -3 dB bandwidth of 215 MHz, a small insertion loss (IL) of 1.881 dB, and a rejection >32 dB. This work paves the way for the realization of wideband acoustic filters operating in the 5G band.

Introduction

Recently, mobile communication systems have continued to demand a high data rate and great mobility^{1–3}. These trends are increasing the need for filters with higher frequencies and wider bandwidths⁴. Emerging 5G, Wi-Fi and 4G LTE communication standards are driving up frequencies from the traditional bands (below 2.6 GHz) to as high as 5 GHz to accommodate wider system bandwidths. Microelectromechanical system (MEMS) filters, such as surface acoustic wave (SAW) and bulk acoustic wave (BAW) filters, are promising candidates for operation at new radio frequency (RF) band sections. However, the SAW filter technology used for current mobile communication systems can hardly achieve frequencies above 3 GHz due to the degraded filter performance and

several fabrication problems caused by the very thin and delicate IDT electrode patterns⁵. BAW filters can provide low insertion loss (IL), good selectivity, and high power handling and are preferred in higher frequency applications^{6–8}.

Two types of technologies, including film bulk acoustic wave resonators (FBARs) and solidly mounted resonators (SMRs), have been used to manufacture thin film BAW filters^{1,8}. SMR devices require a Bragg reflector, preferably patterned with thin-film layers with alternating low and high acoustic impedances. This technology is deemed superior to FBARs in terms of mechanical robustness and power handling. However, the disadvantage of SMRs is an increase in the number of fabrication process steps that should be controlled in terms of film thickness and film properties. For the FBAR, an air cavity is created between the bottom electrode and the carrier wafer. The air/electrode interface can trap more acoustic waves between the electrodes than the Bragg quarter-wavelength acoustic mirror, thus obtaining better effective electromechanical coupling (K_{eff}^2). Furthermore, the FBAR provides a slightly higher Q due to the lack of

Correspondence: Yao Cai (caiyao999@whu.edu.cn) or Chengliang Sun (sunc@whu.edu.cn)

¹The Institute of Technological Sciences, Wuhan University, 430072 Wuhan, China

²Hubei Yangtze Memory Laboratories, 430205 Wuhan, China

Full list of author information is available at the end of the article

© The Author(s) 2022



Open Access This article is licensed under a Creative Commons Attribution 4.0 International License, which permits use, sharing, adaptation, distribution and reproduction in any medium or format, as long as you give appropriate credit to the original author(s) and the source, provide a link to the Creative Commons license, and indicate if changes were made. The images or other third party material in this article are included in the article's Creative Commons license, unless indicated otherwise in a credit line to the material. If material is not included in the article's Creative Commons license and your intended use is not permitted by statutory regulation or exceeds the permitted use, you will need to obtain permission directly from the copyright holder. To view a copy of this license, visit <http://creativecommons.org/licenses/by/4.0/>.

additional reflector layers in which the acoustic wave can be attenuated or can escape.

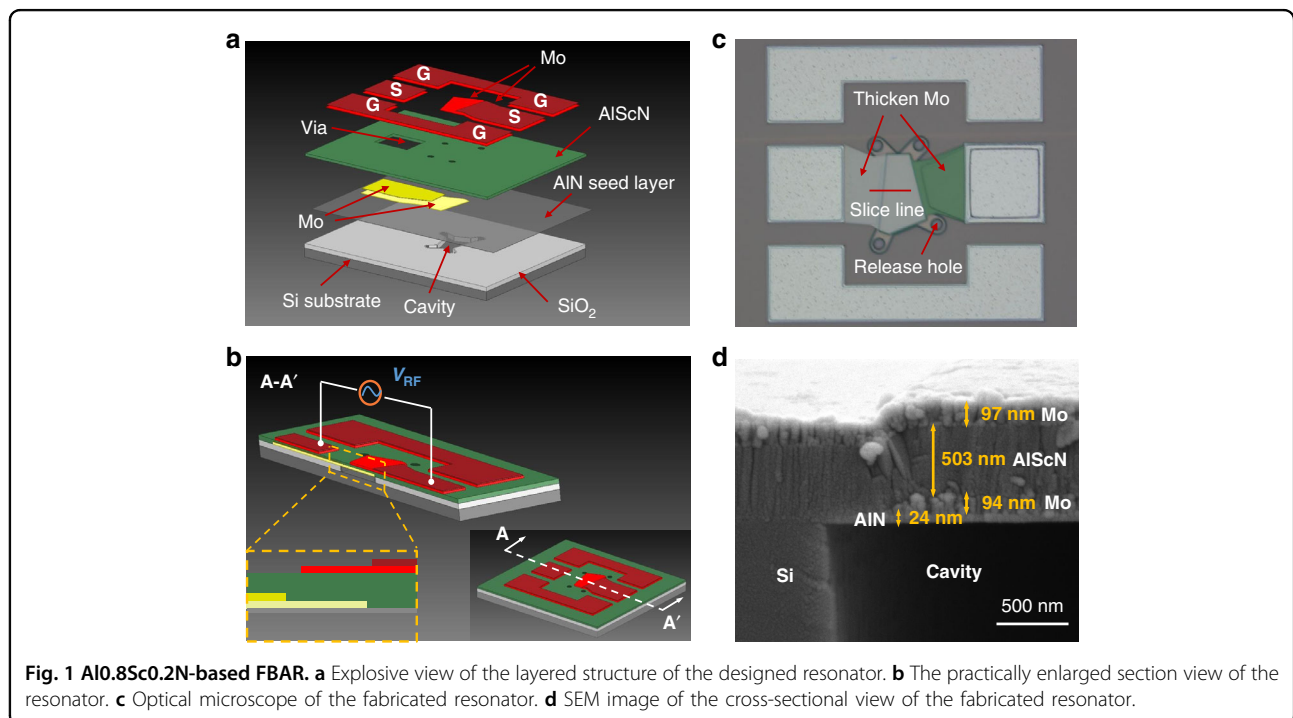
Aluminum nitride (AlN) is utilized in various generations of telecommunications technology due to its high longitudinal sound velocity ν (11,354 m/s), low temperature coefficient of frequency (TCF, -25 ppm/ $^{\circ}$ C), and low acoustic and dielectric losses^{9–11}. Using an optimized FBAR design and a careful choice of materials and non-piezoelectric layer thickness, the K_{eff}^2 of the FBAR can be boosted to values of $\sim 7\%$ ¹². However, new materials with higher electromechanical coupling render potential choices, resulting in relaxed device designs and fabrication margins. $Al_{1-x}Sc_xN$ (AlScN) is one of those materials, which can be deposited through the same means as AlN, that shows an increase in the piezoelectric coefficient. For example, the piezoelectric coefficient d_{33} of $Al_{0.57}Sc_{0.43}N$ is up to five times larger than that of pure AlN^{13–15}. Moreira et al.¹² presented an $Al_{0.85}Sc_{0.15}N$ -based FBAR with a resonant frequency of 2.15 GHz and a K_{eff}^2 of 12.07%. Wang et al.¹⁶ demonstrated a switchable $Al_{0.7}Sc_{0.3}N$ -based FBAR utilizing the newly discovered ferroelectric behavior of $Al_{0.7}Sc_{0.3}N$ thin films.

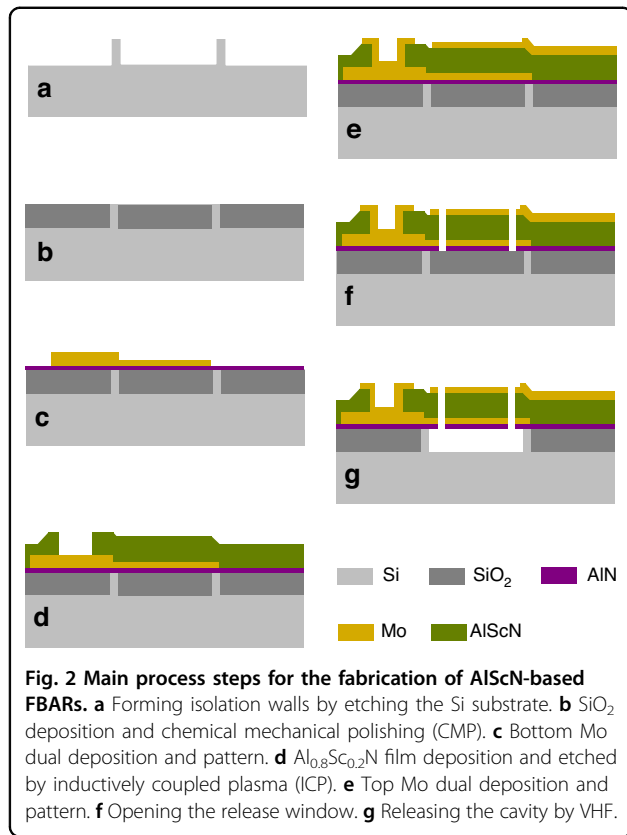
In this work, we report an $Al_{0.8}Sc_{0.2}N$ -based FBAR for the design of acoustic filters. By taking advantage of the high-quality $Al_{0.8}Sc_{0.2}N$ film, the FBAR presents a large K_{eff}^2 of 14.5% and an excellent figure of merit (FOM) of 62. Furthermore, the Mason model is used to extract the important intrinsic material parameters of the $Al_{0.8}Sc_{0.2}N$ film. Subsequently, high- and low-temperature probe stations are employed to study the temperature

characteristics of the $Al_{0.8}Sc_{0.2}N$ -based FBAR. Finally, filters using the $Al_{0.8}Sc_{0.2}N$ film exhibit a center frequency of 4.24 GHz, a -3 dB bandwidth of 215 MHz, a small IL of 1.89 dB, and a rejection above 32 dB. The proposed $Al_{0.8}Sc_{0.2}N$ -based FBAR filters show potential for 5G wideband applications.

Design and fabrication

The designed piezoelectric film bulk acoustic resonator, illustrated in Fig. 1, is composed of six thin films grown on a Si substrate (725 μ m thick). Two additional Mo layers of 120 nm and 37 nm outside the cavity are designed on the top and bottom electrodes, respectively, to reduce electrode resistance. As shown in Fig. 1(a) and (b), the top and bottom electrode layers are patterned to quadrilaterals, and electrical connection strips are used to conduct electrical signals to the pads (S). When an RF signal is applied between the two electrodes of the resonator, longitudinal bulk acoustic waves are excited in the piezoelectric film. Figure 1(d) shows the scanning electron microscopy (SEM) view. Its cross-sectional stack at the slice line is exhibited in Fig. 1(c). On the basis of this design, the proposed AlScN-based FBAR is fabricated utilizing a complementary metal-oxide-semiconductor (CMOS)-compatible microfabrication process involving a combination of seven photolithography masks^{17–19}. The detailed fabrication process is demonstrated in Fig. 2. The fabrication process starts with etching Si to form the isolation walls, which are used to define the cavity. Chemical mechanical polishing (CMP) is used to provide a flat





surface for the deposition of the bottom Mo electrode and piezoelectric AlScN film²⁰. In particular, an isolation wall instead of a swimming pool is used to reduce the difficulty of CMP due to the smaller polished area. Next, a 25 nm-thick AlN seed layer and 100 nm-thick bottom electrode Mo are deposited. Moreover, an additional 120 nm-thick Mo layer is formed on the top surface of the bottom electrode at the position where the opening for the bottom electrode electrical contact will be formed. The presence of the additional Mo layer ensures that the bottom electrode will always retain sufficient thickness after etching the openings in the piezoelectric layer. Then, a 500 nm-thick piezoelectric Al_{0.8}Sc_{0.2}N film is deposited and etched by inductively coupled plasma (ICP) etching to open the bottom electrode. A 100 nm-thick Mo layer is deposited and patterned as the top electrode. Subsequently, a mass loading layer of 37 nm-thick Mo film is deposited and etched above the structure. Finally, the release window is opened, and the whole device is released by a VHF isotropic etcher.

Results and discussion

The cross-sectional transmission electron microscopy (TEM) images are shown in Fig. 3(a) and (b). The Al_{0.8}Sc_{0.2}N film exhibits a good (002) c-axis preferential crystal orientation, which is preferred for achieving a high

Q value for the FBAR^{21,22}. Figure 3(c) shows the electron diffraction pattern of the Al_{0.8}Sc_{0.2}N film in region A of Fig. 3(a). The distance between the two diffracted spots closest to the central spot is 8.345 1/nm, corresponding to a lattice plane (002) spacing of 0.240 nm, which is slightly smaller than that of AlN (0.249 nm). In addition, X-ray diffraction (XRD) 2θ/ω scans of the Al_{0.8}Sc_{0.2}N films include only diffraction maxima attributed to Al_{0.8}Sc_{0.2}N (002), confirming that the Al_{0.8}Sc_{0.2}N layer has a single out-of-plane crystallographic orientation.

The frequency response of Al_{0.8}Sc_{0.2}N-based FBARs is tested in air using a Cascade Microtech GSG probe station (Cascade, America) in conjunction with a network analyzer (N5222B, Agilent Technology). The measured impedance response of the resonator is shown in Fig. 4(a). The K_{eff}^2 of 14.5%, Q_s of 150 and Q_p of 318 are evaluated by²³

$$K_{eff}^2 = \frac{\pi^2 f_s f_p - f_s}{4 f_p f_p} \quad (1)$$

$$Q_{s,p} = \frac{f_{s,p}}{\Delta f_{s,p} - 3dB} \quad (2)$$

where f_s and f_p are the series and parallel resonant frequencies, respectively. The high K_{eff}^2 value of the FBAR is directly related to the enhanced piezoelectric performance with increased Sc content²⁴. The measured result is modeled with the modified Butterworth-Van Dyke (MBVD) model with the circuit shown in the insets in Fig. 4(a). The model consists of a static capacitor C_0 , electrode resistance R_s , dielectric loss R_0 and the motional branches, including a motional resistor R_m , a motional inductor L_m and a motional capacitor C_m ²⁵. The three motional elements in the MBVD circuit can be defined as

$$C_m = C_0 \left(\left(\frac{f_p}{f_s} \right)^2 - 1 \right) \quad (3)$$

$$L_m = \frac{1}{\omega_s^2 C_m} \quad (4)$$

$$R_m = \frac{1}{\omega_s C_m Q_s} \quad (5)$$

where ω_s is the angular resonant frequency ($\omega_s = 2\pi f_s$). The MBVD model fits the measured data with high accuracy, and using Eq. 6, Q_m is calculated to be 424.7. The fitted components are shown in Table 1. Remarkably, due to the thin electrode, the electrode resistance R_s is 1.92 Ω, which is larger than the other two losses. Q_s is strongly influenced by ohmic loss R_s , while at f_p , the loss is negligible, resulting in Q_s being almost half the value of Q_p . Figure 4(b) shows the comparison of the performances of the fabricated FBAR in this work and previous studies^{12,15,16}. The resonator presents

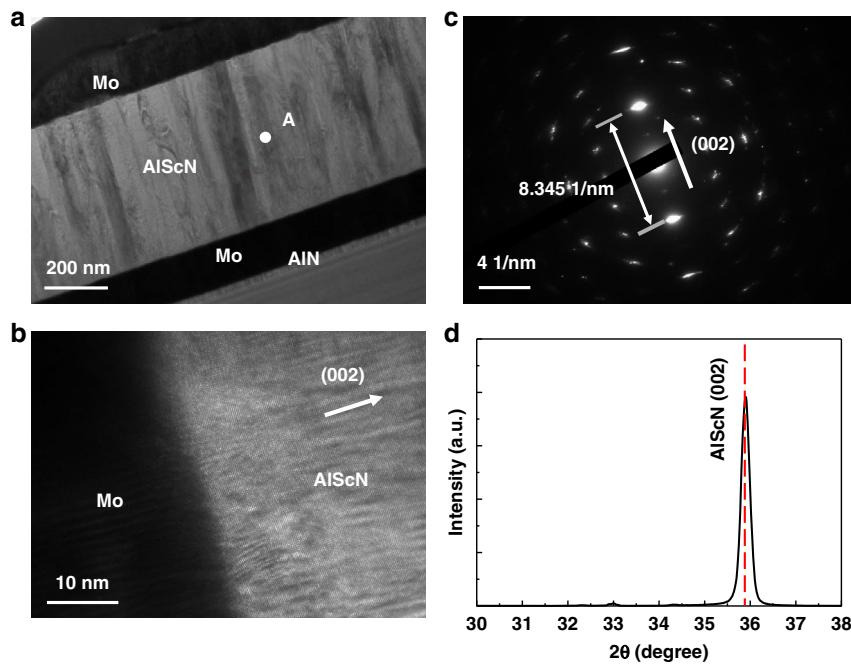


Fig. 3 $\text{Al}_{0.8}\text{Sc}_{0.2}\text{N}$ film characterization. **a** Cross-sectional TEM image of the fabricated FBAR. **b** High-resolution TEM image of the $\text{Al}_{0.8}\text{Sc}_{0.2}\text{N}$ and Mo interface. **c** Electron diffraction pattern of $\text{Al}_{0.8}\text{Sc}_{0.2}\text{N}$ in region A. **d** XRD pattern of the $\text{Al}_{0.8}\text{Sc}_{0.2}\text{N}$ film on a linear scale.

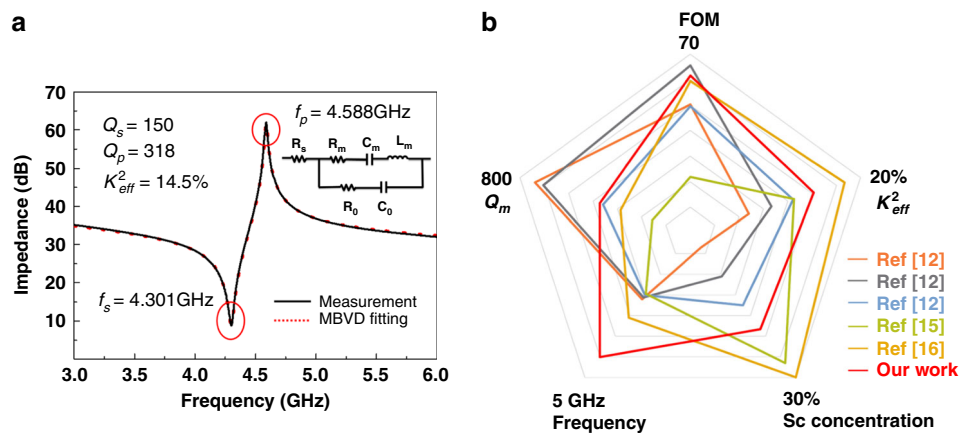


Fig. 4 Experimental results of $\text{Al}_{0.8}\text{Sc}_{0.2}\text{N}$ -based FBAR. **a** Measured and MBVD fitted plot for $\text{Al}_{0.8}\text{Sc}_{0.2}\text{N}$ -based FBAR. **b** Comparison with different studies regarding the performance of AlScN FBAR^{12,15,16}.

the advantage of having a high frequency of 4.3 GHz and an excellent FOM of 62, which is essential for fabricating a 5G wideband filter.

$$Q_m = \frac{1}{R_m} \sqrt{\frac{L_m}{C_m}} \quad (6)$$

To further assess the $\text{Al}_{0.8}\text{Sc}_{0.2}\text{N}$ properties, the Mason model is used to fit the measured data to extract important intrinsic material parameters. Figure 5(a) shows the Mason

model of the FBAR derived from the one-dimensional acoustic wave equation²³. In this model, Z is the characteristic acoustic impedance, k ($k = 2\pi f/\nu$) is the wave-number, d is the thickness of each layer, and $N = k_3 d_3 / (2\pi f k_t^2 C_0 Z_3)$, where k_t^2 is the intrinsic electro-mechanical coupling factor of the $\text{Al}_{0.8}\text{Sc}_{0.2}\text{N}$ film. The bulk material constants for the Mo electrodes and the AlN seed layer are used in this extraction procedure. The layer thicknesses are measured in advance by SEM, as reported in Section II. The acoustic impedance Z and the longitudinal

Table 1 MBVD model parameters.

MBVD Model	R_s (Ω)	R_m (Ω)	C_m (pF)	L_m (nH)	C_o (pF)	R_o (Ω)	Q_m
Value	1.92	0.84	0.10	13.20	0.75	0.85	424.7

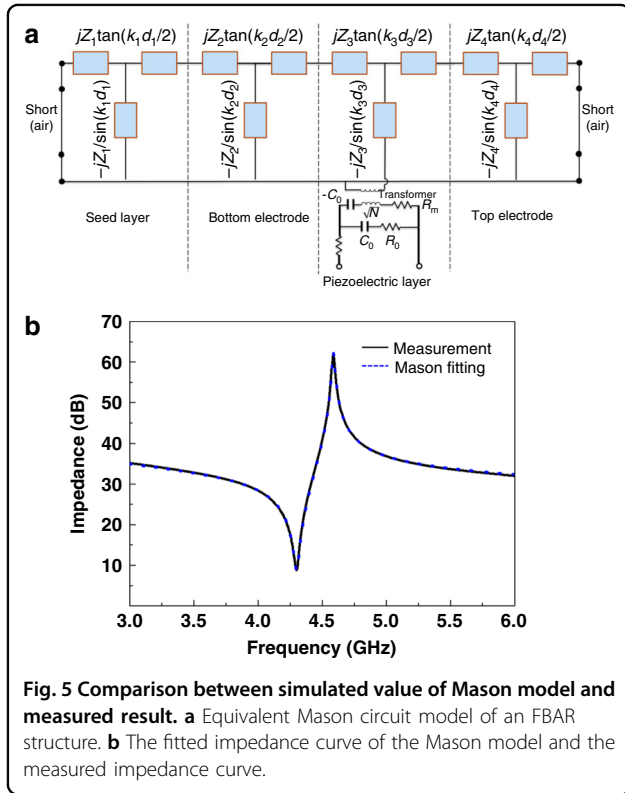


Fig. 5 Comparison between simulated value of Mason model and measured result. **a** Equivalent Mason circuit model of an FBAR structure. **b** The fitted impedance curve of the Mason model and the measured impedance curve.

acoustic velocity v_a are adjusted to fit the f_p of the impedance curve. The intrinsic electromechanical coupling factor K_t^2 is then adjusted to fit the f_s of the curve. The fitted impedance of the Mason model and the measured impedance curve are shown in Fig. 5(b). With the equivalent Mason circuit, we can achieve a very consistent fitting result with the measured impedance. Furthermore, the unknown parameters (ρ , e_{33} , C_{33}^E) can be obtained by^{26,27}.

$$\rho = \frac{Z}{v_a} \tag{7}$$

$$c_{33}^D = \rho v_a^2 \tag{8}$$

$$e_{33} = \sqrt{K_t^2 c_{33}^D \epsilon_r \epsilon_0} \tag{9}$$

$$C_{33}^E = c_{33}^D - \frac{e_{33}^2}{\epsilon_r \epsilon_0} \tag{10}$$

where ρ is the mass density, c_{33}^D is the stiffened elastic constant, e_{33} is the piezoelectric stress constant, C_{33}^E is the elastic constant, and ϵ_r is the relative dielectric

Table 2 Extracted film parameters

Material	K_t^2	ϵ_r	ρ (kg/m ³)	v_a (m/s)	C_{33}^E (Gpa)	e_{33} (C/m ²)
Al _{0.8} Sc _{0.2} N	12.4	13.42	3560	9089	258	2.08

permittivity. The ϵ_r of the Al_{0.8}Sc_{0.2}N film is separately extracted from the static FBAR capacitance C_o , applying the Formula $C_o = \epsilon_r \epsilon_0 A/d$. Here, A is the active FBAR area, and d is the Al_{0.8}Sc_{0.2}N film thickness. Table 2 lists the extracted film parameters of Al_{0.8}Sc_{0.2}N, highlighting a larger e_{33} of 2.08 C/m² than that of AlN (1.55 C/m²)²⁸.

By measuring the frequency responses at different temperatures, the temperature coefficients f_s and f_p of the proposed Al_{0.8}Sc_{0.2}N-based FBAR are found to be -19.2 ppm/°C and -21.1 ppm/°C, respectively, as shown in Fig. 6. TCF is usually an intrinsic property of materials that is dependent on the growth conditions. The TCF of the proposed device is comparable with previously reported values^{29,30}. The difference in TCF between f_s and f_p is caused by a slight shift in K_t^2 since the change in temperature may induce thermal stress in the thin film.

Figure 7(a) and (b) show the SEM image and schematic circuit of the fabricated filter. It consists of 8 elements, including 4 series and 4 shunt resonators. To achieve passband transmit characteristics, a 37 nm Mo mass loading layer is added to the shunt resonator to make its resonant frequency lower than the series resonator. Table 3 summarizes the relevant measured and extracted parameters of the series and shunt resonators used in the filter. Moreover, additional Mo layers are constructed on the interconnect line between each adjacent resonator to improve the performance of the filter. A plot of the measured filter response is shown in Fig. 7(c) and (d). The filter shows a center frequency of 4.24 GHz, a -3 dB bandwidth of 215 MHz, a small IL of 1.881 dB, and a rejection >32 dB. The measured return loss at the center frequency is below -12 dB, indicating a good match to 50Ω without any helper circuits.

Conclusion

In this paper, an Al_{0.8}Sc_{0.2}N-based FBAR is investigated for the design of acoustic MEMS filters. The proposed FBAR devices are yielded by a seven-mask layer wafer process, including sputtering deposition, ICP etching,

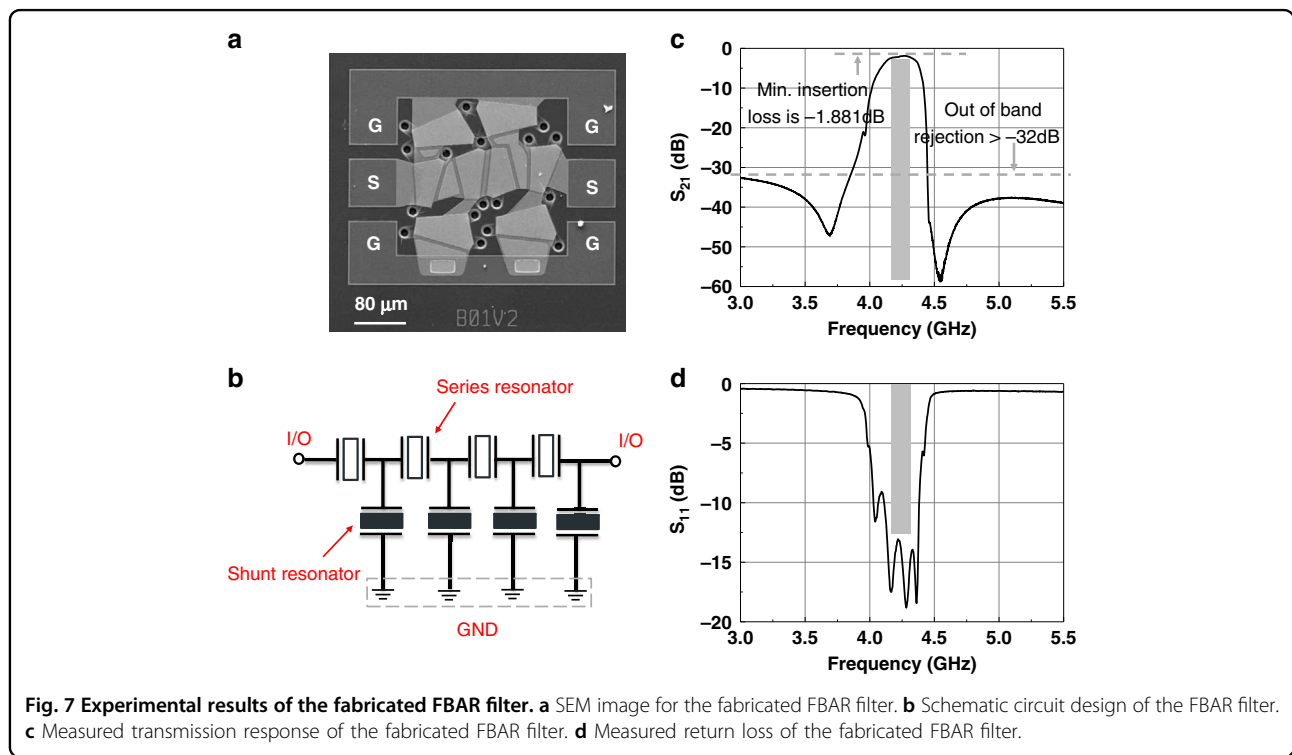
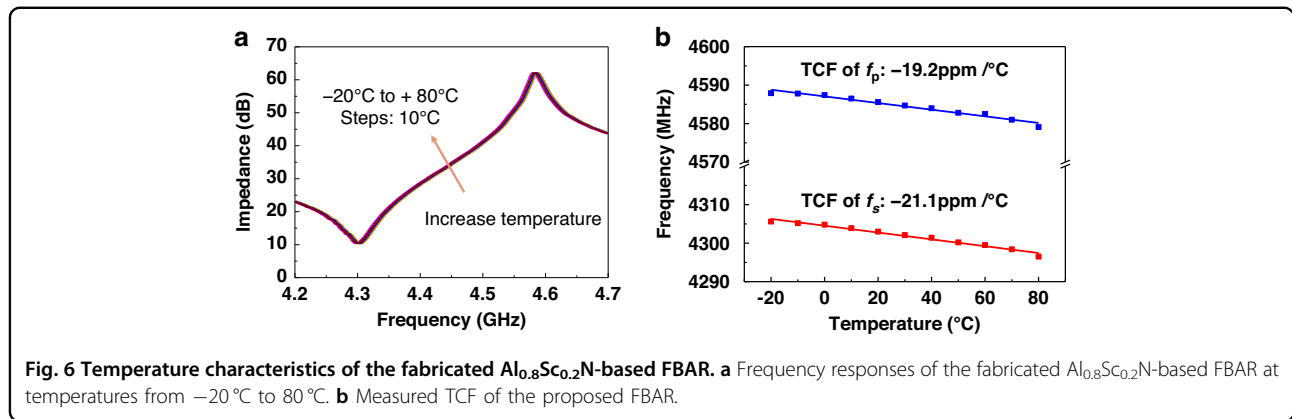


Table 3 Measured and extracted FBAR parameters.

Resonator	A (μm^2)	C_0 (pF)	f_s (GHz)	Q_s	f_p (GHz)	Q_p	K_{eff}^2 (%)
Series	3281	0.75	4.301	150	4.588	318	14.5
Shunt	3794	0.88	4.001	130	4.274	202	14.8

and cavity release. Characterization of the microstructural and crystal structure properties of the sputtered $\text{Al}_{0.8}\text{Sc}_{0.2}\text{N}$ thin film is performed. The results show that the $\text{Al}_{0.8}\text{Sc}_{0.2}\text{N}$ layer has a good c-axis preferential crystal orientation. For the FBAR devices based on the $\text{Al}_{0.8}\text{Sc}_{0.2}\text{N}$ film with a large e_{33} (2.08 C/m^2), a large K_{eff}^2 of 14.5% and an improved FOM of 62 are simultaneously

obtained. Furthermore, the temperature characteristics of the $\text{Al}_{0.8}\text{Sc}_{0.2}\text{N}$ -based FBAR are studied. The TCFs of f_s and f_p of the proposed resonator are found to be $-19.2 \text{ ppm}/^\circ\text{C}$ and $-21.1 \text{ ppm}/^\circ\text{C}$, respectively, indicating excellent temperature stability. The fabricated filter based on the above resonators has a center frequency of 4.24 GHz, a -3 dB bandwidth of 215 MHz, a small IL of

1.881 dB, and a rejection >32 dB, showing the strong potential for 5G RF front-end applications.

Acknowledgements

This work was supported by the Fundamental Research Funds for the Central Universities under Grant No. 2042022kf1027.

Author details

¹The Institute of Technological Sciences, Wuhan University, 430072 Wuhan, China. ²Hubei Yangtze Memory Laboratories, 430205 Wuhan, China. ³School of Microelectronics, Wuhan University, 430072 Wuhan, China

Author contributions

Y.Z. performed the experimental design, simulation and analysis; C.G. and J.Z. contributed to the design of the MEMS mechanism; Y.L., Q.X., and Y.Q. contributed to the device's fabrication; W.L. and J.S. performed the analysis and wrote the paper; Y.C. and C.S. discussed the paper and analysis.

Conflict of interest

The authors declare no competing interests.

Received: 13 May 2022 Revised: 2 September 2022 Accepted: 20 September 2022

Published online: 29 November 2022

References

- Satoh, Y., Nishihara, T., Yokoyama, T., Ueda, M. & Miyashita, T. Development of Piezoelectric Thin Film Resonator and Its Impact on Future Wireless Communication Systems. *Jpn. J. Appl. Phys.* **44**, 2883–2894 (2005).
- Ruby, R. C., Bradley, P., Oshmyansky, Y., Chien, A. and Larson, J. D. "Thin film bulk wave acoustic resonators (FBAR) for wireless applications," in *Proc. IEEE Int. Ultrason. Symp. (IUS)*, 813–821 (2001), <https://doi.org/10.1109/ULTSYM.2001.991846>.
- Chauhan, V. et al. RF Bulk Acoustic Wave Devices: Multiphysical Modeling and Performance. *IEEE Microw. Mag.* **20**, 56–70 (2019).
- Nishihara, T., Yokoyama, T., Miyashita, T. and Satoh, Y., "High performance and miniature thin film bulk acoustic wave filters for 5 GHz," in *Proc. IEEE Int. Ultrason. Symp. (IUS)*, 969–972 (2002), <https://doi.org/10.1109/ULTSYM.2002.1193557>.
- Takai, T. et al., "Investigations on design technologies for SAW quadruplex with narrow duplex gap," in *IEEE MTT-S Int. Microw. Symp.* 1–4 (2016), <https://doi.org/10.1109/MWSYM.2016.7540214>.
- Dubois, M., Billard, C., Muller, C., Parat, G. and Vincent, P., "Integration of high-Q BAW resonators and filters above IC," in *IEEE Int. Digest of Technical Papers. Solid-State Circuits Conference*, 392–606 (2005), <https://doi.org/10.1109/ISSCC.2005.1494034>.
- Piazza, G., Felmetsger, V., Murali, P., Olsson Iii, R. H. & Ruby, R. Piezoelectric aluminum nitride thin films for microelectromechanical systems. *MRS Bull.* **37**, 1051–1061 (2012).
- Ruppel, C. C. W. Acoustic Wave Filter Technology—A Review. *IEEE Trans. Ultrason., Ferroelectr., Freq. control* **64**, 1390–1400 (2017).
- Liu, Y. et al., "Materials, Design, and Characteristics of Bulk Acoustic Wave Resonator: A Review," *Micromachines*, **11**, 2020, <https://doi.org/10.3390/mi11070630>.
- Wingqvist, G. et al. Increased electromechanical coupling in w-Sc_xAl_{1-x}N. *Appl. Phys. Lett.* **97**, 112902 (2010).
- Tajic, A. et al., "No-drift™ BAW-SMR: Over-moded reflector for temperature compensation," in *IEEE Int. Ultrason. Symp. (IUS)*, 1–4 (2016), <https://doi.org/10.1109/ULTSYM.2016.7728616>.
- Moreira, M., Bjurström, J., Katardjev, I. & Yantchev, V. Aluminum scandium nitride thin-film bulk acoustic resonators for wide band applications. *Vac.* **86**, 23–26 (2011).
- Akiyama, M. et al. Enhancement of Piezoelectric Response in Scandium Aluminum Nitride Alloy Thin Films Prepared by Dual Reactive Cosputtering. *Adv. Mater.* **21**, 593–596 (2009).
- Caro, M. A. et al. Piezoelectric coefficients and spontaneous polarization of ScAlN. *J. Phys.: Condens. Matter* **27**, 245901 (2015).
- Schneider, M., DeMiguel-Ramos, M., Flewitt, A. J., Iborra, E. & Schmid, U. Scandium aluminium nitride-based film bulk acoustic resonators. *Proceedings* **1**, 305 (2017).
- Wang, J. et al. A Film Bulk Acoustic Resonator Based on Ferroelectric Aluminum Scandium Nitride Films. *J. Microelectromech. Syst.* **29**, 741–747 (2020).
- Zhu, Y. et al. ScAlN-Based LCAT Mode Resonators Above 2 GHz With High FOM and Reduced Fabrication Complexity. *IEEE Electron Device Lett.* **38**, 1481–1484 (2017).
- Wang, N. et al. Over 10% K_{eff}^2 of demonstrated by 2-GHz spurious mode-free Sc_{0.12}Al_{0.88}N laterally coupled alternating thickness mode resonators. *IEEE Electron Device Lett.* **40**, 957–960 (2019).
- Zhou, J. et al. ScAlN/AlN Film-Based Lamé Mode Resonator With High Effective Electromechanical Coupling Coefficient. *J. Microelectromech. Syst.* **30**, 677–679 (2021).
- Gao, C. et al. "Influence of Etching Trench on K_{eff}^2 of Film Bulk Acoustic Resonator," *Micromachines*, **13**, (2022) <https://doi.org/10.3390/mi13010102>.
- Lloret, F. et al. Diamond underlayer microstructure effect on the orientation of AlN piezoelectric layers for high frequency SAW resonators by TEM. *Microelectron. Eng.* **112**, 193–197 (2013).
- Park, M., Hao, Z., Dargis, R., Clark, A. & Ansari, A. Epitaxial Aluminum Scandium Nitride Super High Frequency Acoustic Resonators. *J. Microelectromech. Syst.* **29**, 490–498 (2020).
- Bi, F. Z. & Barber, B. P. Bulk acoustic wave RF technology. *IEEE Microw. Mag.* **9**, 65–80 (2008).
- Yanagitani, T. & Suzuki, M. Electromechanical coupling and gigahertz elastic properties of ScAlN films near phase boundary. *Appl. Phys. Lett.* **105**, 122907 (2014).
- Larson, J.D., Bradley, P.D., Wartenberg, S. and Ruby, R.C. "Modified Butterworth-Van Dyke circuit for FBAR resonators and automated measurement system," in *Proc. IEEE Int. Ultrason. Symp. (IUS)*, 863–868 (2000), <https://doi.org/10.1109/ULTSYM.2000.922679>.
- Rosenbaum, J.F. *Bulk Acoustic Waves Theory and Devices*. (Artech House, Massachusetts, 1988).
- Hashimoto, K-y. *RF bulk acoustic wave filters for communications*. (Artech House, Massachusetts, 2009).
- Gerfers, F. et al., "Sputtered AlN thin films for piezoelectric MEMS devices-FBAR resonators and accelerometers," in *Solid state circuits technologies*, ed: (IntechOpen, 2010), 333.
- Suzuki, M. and Yanagitani, T. "Temperature coefficient of elastic and GHz piezoelectric properties in ScAlN films," in *Proc. Symp. Ultrason. Electron.*, 253–254 (2013), https://doi.org/10.24492/use.34.0_253.
- Wang, J., Park, M. and Ansari, A. "Thermal Characterization of Ferroelectric Aluminum Scandium Nitride Acoustic Resonators," in *Proc. IEEE Int. Conf. Micro Electro Mech. Syst. (MEMS)*, 214–217 (2021), <https://doi.org/10.1109/MEMS51782.2021.9375203>.